Monthly Notices of the ROYAL ASTRONOMICAL SOCIETY

MNRAS **523,** 6208–6219 (2023) https://doi.org/10.1093/mnras/stad1787
Advance Access publication 2023 June 14

Origin and trends in NH_4^+ observed in the coma of 67P

Z. M. Lewis [1]★ A. Beth,[1] K. Altwegg [2] M. Galand [1] C. Goetz,[3] K. Heritier,[1] L. O'Rourke,[4] M. Rubin [2] and P. Stephenson[1]

[1]*Department of Physics, Imperial College London, Prince Consort Road, London SW7 2AZ, UK*
[2]*Physikalisches Institut, University of Bern, CH-3012 Bern, Switzerland*
[3]*Department of Mathematics, Physics and Electrical Engineering, Northumbria University, Newcastle upon Tyne NE1 8ST, UK*
[4]*ESAC, European Space Agency, Madrid, 28692, Spain*

Accepted 2023 June 9. Received 2023 June 5; in original form 2023 March 2

ABSTRACT

The European Space Agency/Rosetta mission escorted comet 67P/Churyumov–Gerasimenko and witnessed the evolution of its coma from low activity (∼2.5–3.8 au) to rich ion-neutral chemistry (∼1.2–2.0 au). We present an analysis of the ion composition in the coma, focusing on the presence of protonated high proton affinity (HPA) species, in particular NH_4^+. This ion is produced through the protonation of NH_3 and is an indicator of the level of ion-neutral chemistry in the coma. We aim to assess the importance of this process compared with other NH_4^+ sources, such as the dissociation of ammonium salts embedded in dust grains. The analysis of NH_4^+ has been possible thanks to the high mass resolution of the Rosetta Orbiter Spectrometer for Ion and Neutral Analysis/Double Focusing Mass Spectrometer (ROSINA/DFMS). In this work, we examine the NH_4^+ data set alongside data from the Rosetta Plasma Consortium instruments, and against outputs from our in-house ionospheric model. We show that increased comet outgassing around perihelion yields more detections of NH_4^+ and other protonated HPA species, which results from more complex ion-neutral chemistry occurring in the coma. We also reveal a link between the low magnetic field strength associated with the diamagnetic cavity and higher NH_4^+ counts. This suggests that transport inside and outside the diamagnetic cavity is very different, which is consistent with 3D hybrid simulations of the coma: non-radial plasma dynamics outside the diamagnetic cavity is an important factor affecting the ion composition.

Key words: plasmas – methods: data analysis – comets: general.

1 INTRODUCTION

Protonated ammonia (NH_4^+) is a key ion species in the cometary coma, since it can only be formed through ion-neutral chemistry (i.e. not directly through photoionization). The neutral gas coma is primarily comprised of sublimated water (and carbon dioxide to a lesser extent) ice, which is then photoionized by solar extreme ultraviolet (EUV) photons and electron impact to produce H_2O^+. Since H_2O has a higher proton affinity than OH, it is energetically favourable for a proton to be transferred, such that H_3O^+ is formed, and this is generally the dominant ion species in the cometary ionosphere at intermediate/high activity. However, when the outgassing is sufficiently high, other neutral species with higher proton affinity than H_2O readily become protonated. We shall refer to such molecules as high proton affinity (HPA) species. Of the neutral species known to be abundant in cometary comae, NH_3 has the highest proton affinity, so NH_4^+ is the terminal ion species; all proton transfer reaction pathways lead to it, and it is therefore a good tracer of how much ion-neutral chemistry took place before transport or dissociative recombination takes over as the dominant plasma loss process. When the outgassing is high enough, NH_4^+ is expected to be the dominant ion species in the dense inner coma (e.g. Aikin 1974; Vigren & Galand 2013; Heritier et al. 2017).

The *Giotto* spacecraft, which conducted a fly-by of comet 1P/Halley in 1986 March, carried an Ion Mass Spectrometer (IMS; Balsiger et al. 1986). This instrument identified the presence of a mass peak at 18 *m*/*z*, but did not have sufficient mass resolution to distinguish NH_4^+ from H_2O^+, requiring instead the use of ionospheric modelling to interpret the data (e.g. Altwegg et al. 1993; Häberli et al. 1995; Rubin et al. 2009). In contrast, the European Space Agency (ESA)/Rosetta mission escorted comet 67P for 2 yr, capturing high-resolution (HR) ion and neutral mass spectra with the Rosetta Orbiter Spectrometer for Ion and Neutral Analysis/Double Focusing Mass Spectrometer (ROSINA/DFMS; Balsiger et al. 2007). Its high mass resolution ion mode allowed direct unambiguous detection of the NH_4^+ for the first time (Beth et al. 2016), as well as the detection of other protonated HPA species (Heritier et al. 2017; Beth et al. 2020). The goal of this study is to exploit the DFMS HR ion mode data set in depth over the 2-yr escort phase of Rosetta, focusing on the presence of NH_4^+, to confirm its source in the coma, and to understand what factors drive its abundance.

Aside from protonation of NH_3, which is the dominant pathway to NH_4^+ via ion-neutral chemistry, another possible source of NH_4^+ is the dissociation of ammonium salts embedded in dust grains (predominantly $NH_4^+SH^-$, but a host of others have been detected; Altwegg et al. 2020). The exact mechanism by which the ammonium

★ E-mail: z.lewis21@imperial.ac.uk

salts could directly lead to the formation of NH_4^+ is uncertain, but it is possible that they could dissociate into a cation–anion pair directly following either sublimation or electron impact. In the case of measurements at comet 67P, this could occur either in the coma or inside the DFMS instrument (Hänni et al. 2019). In both cases, electric fields may be involved in separating the two. Dissociation into neutral NH_3 and H_2S is, however, more likely, and happens either during or after sublimation of the salt. The salts were identified from the detection of NH_3 peaks coinciding with H_2S peaks in the neutral mode of DFMS (Altwegg et al. 2022) above the background coma level; thus, it is not possible to directly relate them to individual detections of NH_4^+ in ion mode, which could not be operated at the same time. Detections of ammonium salts are also biased towards lower outgassing where there can be a clearer signal above the background. If sublimation of salts into cation and anion pairs was an important process, we would expect to see anions detected by Ion and Electron Sensor (IES), which is not the case, though they could be repelled by the negative spacecraft potential. We therefore cannot exclude a dust source for NH_4^+. One of the goals of this study is to confirm whether the ion-neutral chemistry is the main contributor to NH_4^+ compared with the possible dust origin.

NH_4^+ was previously detected near perihelion (Beth et al. 2016; Heritier et al. 2017). During this period, the outgassing of 67P was high enough to have a diamagnetic cavity formed (Rubin et al. 2012). Rosetta crossed over into this magnetic field-free region a total of 713 times (Goetz et al. 2016a), measuring clear periods of close to zero magnetic field with the Rosetta Plasma Consortium Magnetometer (RPC/MAG) instrument (Glassmeier et al. 2007). Cavity signatures were identified from heliocentric distances of 2 au inbound to perihelion (1.24 au), up to 2.4 au outbound (between 2015 April and 2016 February), and when local outgassing was above 10^{27} s^{-1} (Goetz et al. 2016b). The plasma characteristics were found to be systematically different inside the diamagnetic cavity, with less variation in the plasma density (Henri et al. 2017) and ion bulk velocity (Odelstad et al. 2018) than outside. A population of cold ($<$10 eV) electrons was also more consistently observed in the cavity, leading to a smaller flux of electrons to the spacecraft surface and a less negative spacecraft potential (Odelstad et al. 2018). Odelstad et al. (2018) found the ion bulk velocities to be mostly radial within the cavity, with enhanced dynamics outside. This was also predicted by hybrid modelling in Koenders et al. (2015), who showed that the anticometward radial velocity dominates the flow inside the diamagnetic cavity, with more tailward flow present outside. The ion composition in and out of the diamagnetic cavity has, however, not been looked at yet at 67P. Here, we assess any change between these regions, taking advantage of the high mass resolution ion mode of DFMS, and focusing on the chemistry tracer, NH_4^+.

In order to identify the source of NH_4^+ in the coma, we have used a multi-instrument data set from ROSINA (Section 2.1) and Rosetta Plasma Consortium (RPC; Section 2.2). The ionospheric model used to interpret the ion data is presented in Section 2.3. We then examine the trends in NH_4^+ detection throughout the Rosetta escort phase, as well as the trend for other protonated HPA species (Section 3.1), and compare them to changes in local outgassing, NH_3 mixing ratio, and spacecraft latitude (Section 3.2). In Section 4, we assess the dependence of NH_4^+ detection on the magnetic field strength, through a case study of 2015 July 29 (Section 4.1), extended to other days with both HR ion mode data and diamagnetic cavity crossings (Section 4.2). Finally, in Section 4.3, we present a comparison with the ionospheric model for two key periods during which both the cavity and NH_4^+ were observed. The outcome of our study is discussed in Section 5.

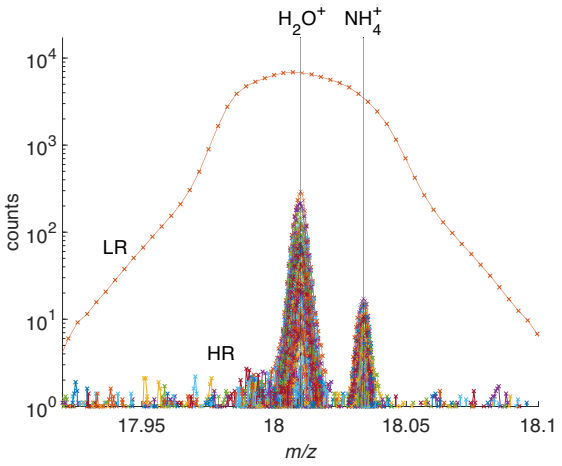

Figure 1. DFMS mass spectra from 2015 July (channel A), from the HR and LR demonstrating the separation of H_2O^+ and NH_4^+ in the HR mode.

2 METHODS

2.1 ROSINA

2.1.1 DFMS

IMS data used in this study are from ROSINA/DFMS, described in detail in Balsiger et al. (2007). The instrument measures the mass per charge ratio of ions hitting the detector, in both high and low mass resolution modes. In neutral mode, the gas is first ionized within the gas chamber through electron impact from electrons emitted by a filament before it can be analysed and the bias voltage of the source prevents external coma ions from making it through the analyser section of the instrument. Both features are switched off during ion mode. The instrument is therefore not able to measure both ions and neutrals simultaneously. In this study, we use data from both modes.

The mass per charge range is 13–150 a.m.u. per charge (m/z), though the actual mass range scanned at a given time has been changed to adjust to different conditions throughout the mission (i.e. scanning the higher mass ions only when close enough to perihelion when significant chemistry occurs). It takes 10 s to set the voltages for each integer m/z, followed by 20 s of integration time. The two resolutions offered by DFMS [HR where $m/\Delta m > 3000$ and low resolution (LR) where $m/\Delta m \approx 500$ at 1 per cent peak height] are also advantageous at different times. On the one hand, HR mode is able to distinguish between masses of the same integer mass per charge, and is more useful at higher local ion fluxes. On the other hand, the LR mode is more sensitive, so can detect lower ion fluxes, albeit without mass separation at a given mass per charge. In this study, we mainly use ion data from the HR mode, as it is required to separate NH_4^+ from H_2O^+, both at 18 m/z, as illustrated in Fig. 1.

First, we sum the counts over a 0.02 m/z range away from where any mass peaks are expected (17.94–17.96 m/z for 18 m/z) to find a background count level. This level is then compared to the counts summed over a $\pm$0.01 m/z window at the expected peak location (e.g. 18.033 83 m/z for NH_4^+). If the count sum at the peak is five times higher than the background level in both channels, we consider the ion species to be detected. Where count sums are referred to in this paper, this refers to the peak count sum with the background subtracted. The count sums from channels A and B are added together, unless specified otherwise. The background is generally very low in HR mode at the lower mass/charge ratios,

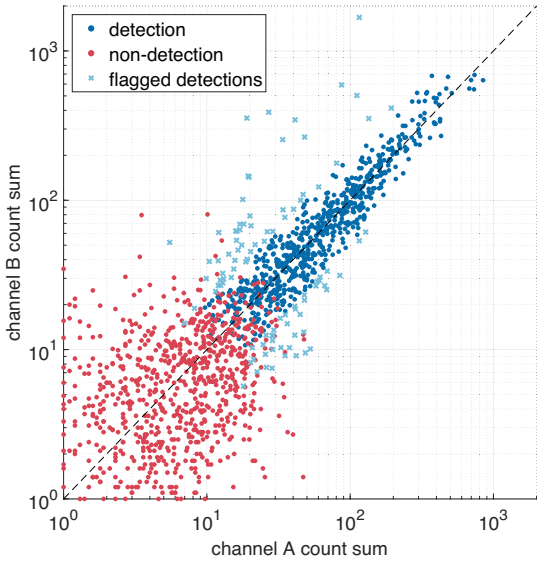

Figure 2. Count sums over the NH_4^+ peak from the two channels of DFMS (A and B), where red showing non-detections of the ion species and blue showing identified detections. The light blue crosses show where detections have been discounted due to large (> 50 per cent) difference between the count sums from the two channels.

typically 2–6 counts at 18 *m*/*z*, but increases significantly at higher mass/charge ratios. The DFMS counts cannot be simply translated into ion number densities since whether or not an ion is detected depends on other factors, such as the spacecraft potential and DFMS field-of-view orientation with respect to the nadir direction. For this reason, a quantitative description of how the NH_4^+ density varies in e.g. cometocentric distance, or direct, quantitative comparison with the ion densities computed by the ionospheric model (see Section 2.3), is beyond the scope of this study. However, a rough estimation of a minimum detectable threshold for detection of NH_4^+ by DFMS is discussed in Appendix A.

The ROSINA instruments are known to be affected by contamination from the spacecraft outgassing (Schläppi et al. 2010). Specifically, the propellant monomethylhydrazine (CH_3NHNH_2) can result in false-positive detections of NH_4^+ (Beth et al. 2016). To mitigate the majority of this effect on the data set used in this study, DFMS ion mode scans taken within 1 hour after a wheel offloading manoeuvre (when the thrusters are fired to decelerate the reaction wheels) were flagged and subsequently removed. We also remove scans for which the difference in the count sums between the two channels A and B is greater than 50 % (see Fig. 2), and for which the field of view of DFMS is off-nadir (nadir direction $<10^\circ$ from the centre of the 20° field of view of DFMS).

We use the neutral composition data set, to assess the NH_3 neutral density, which is derived by combining the volume mixing ratio from the DFMS mass spectrometer with the total neutral density from the Comet Pressure Sensor (COPS; Gasc et al. 2017).

2.1.2 COPS

We use total neutral density from the ROSINA/COPS instrument (Balsiger et al. 2007). It comprises two pressure gauges, the 'nude gauge' and the 'ram gauge'. The nude gauge measures the total neutral particle density of the gas, while the ram gauge measures cometary gas flux via the ram pressure. They operate by ionizing the incoming neutral gas with 150 eV electrons and then measuring the resulting ion current. Both gauges are mounted on the end of 25 cm booms to reduce the influence of molecules scattered off the surface of Rosetta. The total neutral density can then be derived, and has to be corrected for the neutral composition (obtained from DFMS), as the efficiency of the detection process varies with neutral species (Gasc et al. 2017).

The total neutral density can also be combined with neutral composition from DFMS to derive individual species densities (Gasc et al. 2017). In this study, we frequently use a proxy for the local outgassing, $Q_{\rm loc}$, derived from the conservation of the neutral flux initially produced from the surface:

$$Q_{\rm loc} \sim 4\pi u_{\rm n} n_{\rm n} r^2 \ ({\rm s}^{-1}), \tag{1}$$

where $u_{\rm n}$ is the neutral bulk velocity, assumed to be 700 m s^{-1}, r is the comet–spacecraft distance, and $n_{\rm n}$ is the total neutral density measured by COPS at cometocentric distance r.

2.2 RPC

In this study, the magnetic field and spacecraft potential data are provided by the RPC (Carr et al. 2007) Magnetometer (RPC/MAG; Glassmeier et al. 2007) and Langmuir Probe (RPC/LAP; Eriksson et al. 2007) instruments, respectively.

RPC/MAG is a fluxgate magnetometer, comprised of two sensors, inboard (IB) and outboard (OB) mounted along a 1.5 m boom. The IB sensor is closer to the spacecraft than the OB sensor, therefore more affected by spacecraft disturbance. For this reason, in this study we use data from the OB sensor only. MAG is calibrated by setting the mean field within the diamagnetic cavity to 0 nT (Goetz et al. 2016a). Both sensors have two modes, normal (1 Hz) and burst (20 Hz), to allow for different sampling rates at different locations, though OB was always in burst mode on the days used in this study. For this study, we resample the burst mode data to 1 Hz, as we focus on the 'background' magnetic field and not the smaller scale fluctuations. To interpolate the magnetic field strength to the DFMS scan times, we take the mean magnitude of the field over the 20 s integration period. To remove the data set when the magnetic field is highly variable over the period of integration, for example when a steepened magnetosonic wave is present (Ostaszewski et al. 2021), we then remove integrated data points with a standard deviation >3 nT over the 20 s period.

The spacecraft potential is derived from the RPC/LAP making voltage 'sweeps', altering the potential difference between the spherical probes. The voltage at which the probe becomes positive with respect to the surrounding plasma is identifiable in the *V–I* characteristic from the probe, as the photoemission current decreases exponentially to zero once the photoelectrons begin to be attracted back to its surface. The spacecraft potential of Rosetta was usually negative, and linked to the large warm electron population (Odelstad et al. 2017). It may then influence the IMS data from DFMS: a negative potential can accelerate positive ions towards the instrument, pushing them out of the energy acceptance range of DFMS. We assess this potential effect in Section 4.1.

2.3 Ionospheric model

The model first described in Heritier et al. (2017) solves a set of coupled continuity equations to find $n_j(r)$, the number density of ion species j at a given cometocentric distance, r. The continuity equation is given by

$$\frac{\partial n_j(r,t)}{\partial t} + \nabla \cdot (n_j(r,t)\boldsymbol{u}_j(r)) = P_j(r,t) - L'_j(r,t) n_j(r,t), \tag{2}$$

where $\boldsymbol{u}_j(r)$ is the bulk velocity of the species j at r, $P_j(r, t)$ is the production rate of ion species j, including the photoionization and electron impact rates (Galand et al. 2016; Stephenson et al. 2023) and ion-neutral reactions. The photoionization rate is calculated using the attenuated solar EUV spectrum (assessed by solving the Beer–Lambert law), combined with the photoionization cross-sections for each neutral species, DFMS neutral composition, and COPS total neutral density. The electron impact ionization rate is derived from the associated cross-sections, the suprathermal electron spectral flux (from RPC/IES; Burch et al. 2007), DFMS neutral composition, and the COPS total neutral density. The chemical production rates are derived from the reaction coefficients for the production of ions through ion-neutral interactions and the associated neutral and ion densities of the reactants. $L'_j(r, t)$ gives the loss rate of ion species j, through both ion-neutral chemistry and ion–electron dissociative recombination (reactions where an ion and electron combine to form neutral species). The equations are solved for spherical shells of the coma, starting at the shell adjacent to the cometary surface where there is no transport from below. The model assumes no electric or magnetic fields, and non-radial ion dynamics are not included. This is discussed further in Section 4.3.

For Section 4.3, we ran the ionospheric model using the COPS total neutral density, DFMS neutral composition, cometocentric distance, and heliocentric distance as inputs. First, the neutral density and composition were filtered to remove data taken up to 30 min after a wheel offloading manoeuvre, or when the comet and solar aspect angles indicated off-nadir spacecraft (and hence DFMS) pointing. Then, a median filter was applied to the COPS neutral density to remove remaining sharp peaks (due to, e.g. dust impacts). Means were taken over a 12.4 h window, to smoothen the effect of the comet rotation, and windows with insufficient data availability were removed. The model was first run for each 12.4 h window with all ion-neutral reactions included (see Heritier et al. 2017). We then removed direct pathways to NH_4^+ from non-water species, to see the relative contribution of reactions of NH_3 with other protonated HPA species compared to those from H_2O^+ and H_3O^+.

3 NH_4^+ THROUGHOUT THE ESCORT PHASE

In order to shed more light on the source of NH_4^+, we examine its abundance variation during the escort phase, and with outgassing rate, and in terms of latitude, season, and neutral composition. We support observations from ROSINA (see Section 2.1) with outputs from ionospheric modelling (see Section 2.3), to confirm that the ion species is produced within the coma (i.e. through ion-neutral chemistry or dust grain impact), and not solely from spacecraft outgassing. In this section, we do not distinguish between data points inside and outside the diamagnetic cavity.

3.1 HPA detection trends throughout the mission

Fig. 3 shows how the occurrence frequencies (detections/scans) of NH_4^+ and H_3O^+ detections change throughout the escort phase, as well as those of other HPA species. The total counts over the NH_4^+ mass peaks are also assessed. Generally, the occurrence of NH_4^+ follows the outgassing rate, when the change in cometocentric distance is taken into account. It peaks in 2015 August when 67P was close to perihelion. The higher outgassing leads to a denser coma with more frequent chemical reactions that pave the way for richer ion chemistry with multiple protonated HPA species. Fig. 3(b) shows the detection of three other protonated HPA species: H_2COH^+, $CH_3OH_2^+$, and H_3S^+. H_2COH^+ and $CH_3OH_2^+$ need to be examined in the HR mode of DFMS to distinguish them from other ions at the same mass per charge (Heritier et al. 2017; Beth et al. 2020). H_3S^+ is the only ion species at 35 m/z, and hence LR can be also used to take advantage of its higher sensitivity. These ion species are predominantly detected around perihelion in 2015 July, August, and September and are an indicator that more complex ion-neutral chemistry was occurring during this time (see Section 4.3).

A notable exception in the pattern of NH_4^+ occurrence frequency and mean count sum is 2015 March, which exhibits significantly higher values than expected compared to the surrounding months, and for this heliocentric distance (2 au). HR ion mode data for this month were available for March 3, 4, and 7, but after removing detections that may have been affected by spacecraft outgassing, the majority of remaining detections occur on March 3. The reason for the high counts on this day remains unclear, but the local outgassing also increases by around an order of magnitude between 2015 February and March (Fig. 3a). This will be discussed further in Section 5.

Fig. 4 shows the NH_4^+ count sum as a function of local outgassing, colour-coded by the time along the mission. There is no clear correlation below 2×10^{27} s^{-1}. Above, the count sum generally increases with increasing local outgassing. This suggests again that during the period around perihelion (purple markers), NH_4^+ is being produced through chemistry in the coma, driven by increasing neutral densities, or by dust grain impacts that also increase with outgassing. High NH_4^+ count sums at lower outgassing levels mainly occur pre- or post-perihelion and could be attributed to potentially remaining spacecraft outgassing (we have mitigated most of the impact of spacecraft outgassing by removing data up to 1 h after a wheel offloading manoeuvre) or more erratic dust grain impacts. No dependence in cometocentric distance or DFMS channel could be identified.

Fig. 5(a) shows the same as in Fig. 4 but for 2015 July and August only. We see that while there is an overall trend for higher NH_4^+ count sums at higher outgassing, on shorter time-scale the count sums can vary highly for little change in outgassing. Fig. 5(b) shows NH_4^+ count sum against NH_3 mixing ratio for the same time period; there is no clear trend. This suggests that the NH_4^+ production is primarily driven by the local outgassing rate (and therefore the density and likelihood of ion-neutral collisions), rather than the amount of NH_3 present.

3.2 Latitudinal heterogeneities

Hemispheric heterogeneities in coma composition and outgassing of the surface are well described (e.g. Hässig et al. 2015; Le Roy et al. 2015; Gasc et al. 2017) and determined primarily by season changes in solar insolation, as well as some inhomogeneity of the surface (Fougere et al. 2016). Here, we examine these variations for NH_4^+, comparing them to the mean NH_3 number density, and mean local outgassing. Fig. 6 shows each of these quantities separated into latitudinal bins for the northern hemisphere (NH) autumn/ southern hemisphere (SH) spring season described in Table 1.

NH autumn/SH spring (Fig. 6) corresponds to the period around perihelion, and the highest detection rate of NH_4^+ is observed over both hemispheres. The Southern hemisphere has up to 10 times higher local outgassing than the Northern hemisphere, and also larger NH_3 number densities. The proportion of 18 m/z scans resulting in a detection of NH_4^+ is therefore also significantly higher above the Southern hemisphere (see Fig. 6a), as the higher neutral density permits more ion-neutral interactions (and also more dust impacts). The sharp drop in local outgassing at $-60°$ is due to the time at which Rosetta flew over these latitudes: latitudes of $-60°$ to $-80°$ were only passed over in 2015 July, when 67P was at 1.5 au and the

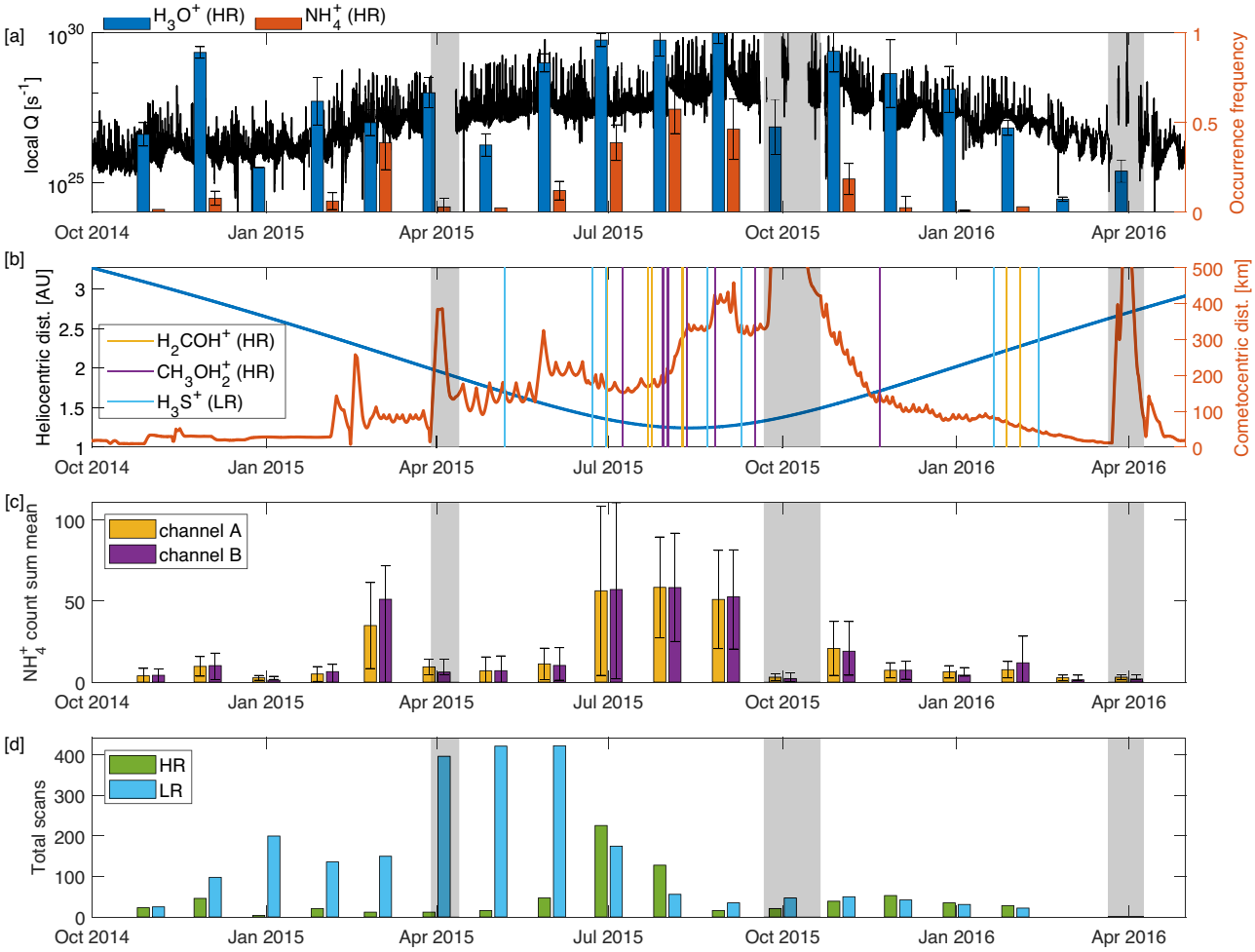

Figure 3. (a) Normalized occurrence frequency of H_3O^+ and NH_4^+ detections by ROSINA/DFMS per month during the escort phase, with local outgassing estimate from ROSINA/COPS. Error bars show the variation in the occurrence frequency as the detection threshold is altered. (b) Heliocentric (black) and cometocentric (orange) distances, during the escort phase with vertical lines representing the detection of three HPA ions by ROSINA/DFMS. (c) Mean of the count sums for NH_4^+ each month in the two channels of the detector. Error bars show the standard deviation. (d) Scans per month in HR and LR modes of DFMS for context. Excursions (2015 September/October and 2016 April) and safe mode (2015 April) are shaded in grey.

local outgassing was 10 times less than in 2015 August. When 67P was at perihelion (1.25 au), it flew over more equatorial regions.

In this section, we have confirmed that NH_4^+ is produced in the cometary coma, by showing its increasing prevalence as the outgassing increases near perihelion. We also show that other HPA species appear more frequently near perihelion, suggesting that the ion-neutral chemical reactions leading to production of these species, and ultimately to NH_4^+, happen more readily at this time. However, from these data we cannot conclude whether NH_4^+ production is driven more by ion-neutral chemistry or by impacting dust grains with ammonium salts embedded. Dust activity increases with outgassing, as does coma density and the possibility of ion-neutral chemistry.

4 NH_4^+ IN THE DIAMAGNETIC CAVITY

It is clear from the data presented in Section 3 that, to first order, the production of NH_4^+ is driven by increased local outgassing, with the highest rates of detection around perihelion over the Southern hemisphere. We now focus on the period close to perihelion, during which the diamagnetic cavity was frequently detected (Goetz et al. 2016a). We compare the measured NH_4^+ count sums with the magnetic field magnitude from RPC/MAG (see Section 2.2) in order to identify the main source of NH_4^+.

4.1 Case study: 2015 July 29

Fig. 7 shows the spectra for all the scans of 18 m/z by ROSINA/DFMS in HR ion mode on 2015 July 29. This was the day with the most HR ion mode data collected within the diamagnetic cavity, therefore it is useful for this study (see Table 2). The cometocentric distance of Rosetta varied between 182 and 193 km during the time that the HR ion mode of DFMS was on (07:12-19:38 UTC), and Rosetta was above the Southern hemisphere of 67P between −40° and −45° latitude. The comet was around 2 weeks before perihelion, at a heliocentric distance of 1.26 au.

In Fig. 7, the spectra are colour-coded by the mean absolute magnitude of the magnetic field (from RPC/MAG) during the integration time of ROSINA/DFMS (20 s), therefore the spectra taken within the cavity are shown in the darkest blue. This colour scheme reveals that the strongest NH_4^+ spectra are usually observed in or close to the diamagnetic cavity, and weaker signatures are

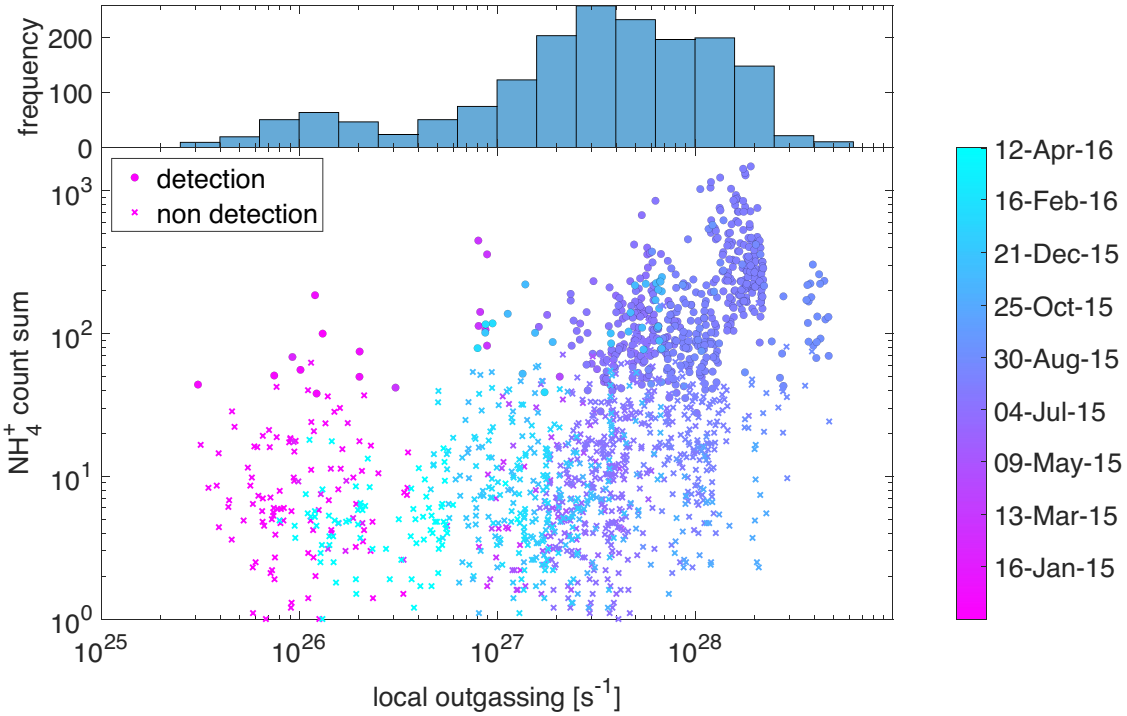

Figure 4. (Top) Histogram showing number of points in each outgassing bin. (Bottom) NH_4^+ count sum against local outgassing, with the colour scale showing the time along the mission. The circles show where NH_4^+ is considered to be detected, and the crosses show where it is not.

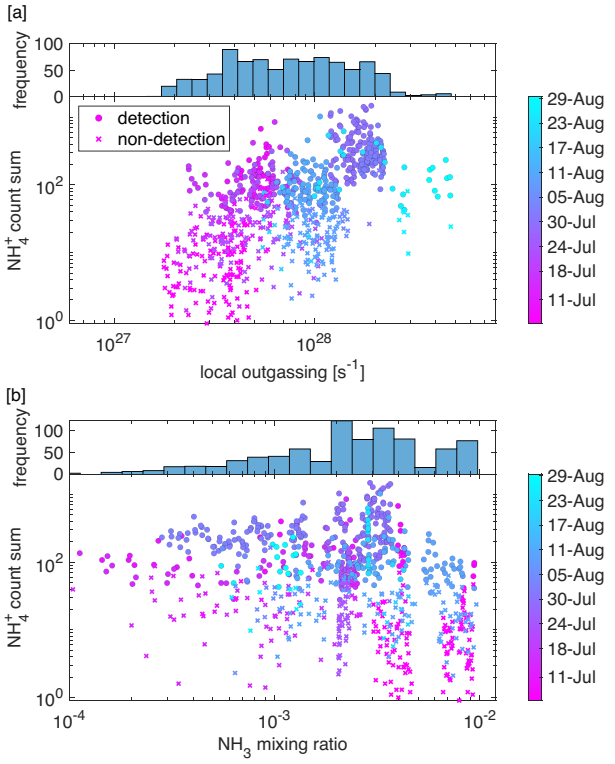

Figure 5. (a) (Top) Histogram showing the distribution of data in each local outgassing bin. (Bottom) NH_4^+ count sum against local outgassing. (b) (Top) Histogram showing distribution of data in each NH_3 mixing ratio bin. (Bottom) NH_4^+ count sum against NH_3 mixing ratios. Points are coloured by time, for 2015 July and August.

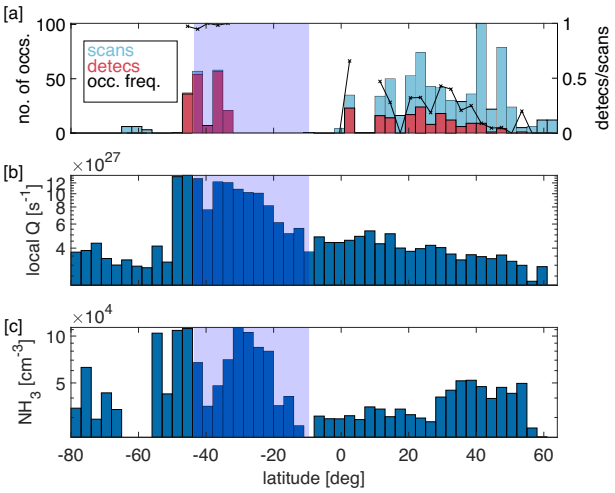

Figure 6. Number of mass 18 m/z scans in HR by ROSINA/DFMS and NH_4^+ detections (a), local outgassing (b), and mean NH_3 number density (c) separated into latitudinal bins for the NH autumn/SH spring season (see Table 1). The violet shaded region shows the range of subsolar latitudes over the season.

Table 1. Seasonal variations during the escort phase (Heritier et al. 2018).

Interval	Season	Heliocentric dist. (au)
01/08/2014–10/05/2015	NH summer/SH winter	3.60–1.67
10/05/2015–04/09/2015	NH autumn/SH spring	1.67–1.25, 1.25–1.27
04/09/2015–21/03/2016	NH winter/SH summer	1.27–3.05

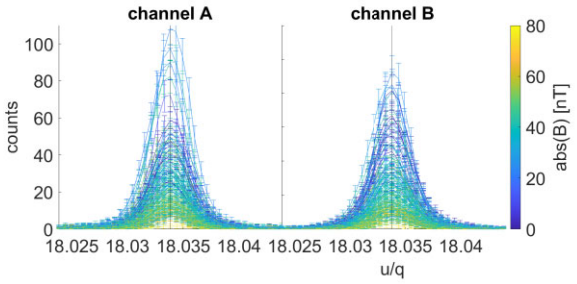

Figure 7. All HR ion mode spectra from ROSINA/DFMS at the location of NH_4^+ on 2015 July 29. The colour scale shows the mean magnetic field magnitude (in nT) from RPC/MAG over the 20-s scan time.

Table 2. Cavity crossings with HR ion mode data. Highlighted rows contain scans of 18 *m*/*z*. Cavity crossing list is taken from Goetz et al. (2016b).

Date	Start (hh:mm:ss)	End (hh:mm:ss)	Duration (mm:ss)	HR masses (*m*/*z*)
2015-07-08	17:15:50	17:22:36	06:46	34–47
2015-07-29	**13:21:38**	**13:28:41**	**07:03**	**17–30**
	13:58:06	**13:58:58**	**00:52**	**18**
	14:19:00	**14:19:48**	**00:48**	**18**
	14:34:21	14:37:29	03:08	44–50
	14:57:31	**15:07:09**	**09:38**	**18, 13–27, 50**
	16:41:45	**16:45:51**	**04:06**	**17–24**
2015-08-09	10:22:50	10:24:33	01:43	29–32
2015-08-22	06:52:09	06:54:04	01:55	38–41
2015-11-21	07:28:49	07:30:35	01:14	25–27
	07:32:18	07:33:14	00:56	33
	07:37:55	07:38:57	01:02	45
	07:55:42	07:56:46	01:04	40–41
	08:04:43	**08:08:56**	**04:13**	**16–24**
	08:33:04	08:33:38	00:34	34
2015-11-25	**07:29:21**	**07:30:53**	**01:32**	**17–19**
	08:00:54	08:01:24	00:30	No full scans

mostly found where the magnetic field magnitude is higher ($|B| \geq$ 40 nT).

In Fig. 8, the first cavity crossing occurs at 13:21–13:28, shortly before which there is a jump in the NH_4^+ counts, and afterwards the counts decrease again. The counts are then elevated again during the subsequent boundary crossings at 13:58, 14:19, 14:34, and 14:57, and again at 16:41. However, there are several instances when Rosetta is outside the diamagnetic cavity, and there is no wheel offloading manoeuvre, sudden increase in local outgassing, or sudden change in cometocentric distance to explain the elevated counts. It is not clear what the origin of these enhanced NH_4^+ spectra is.

Fig. 9 shows the NH_4^+ count sums against magnetic field magnitude (a), cometocentric distance (b), and spacecraft potential (d), as well as the dependence of the spacecraft potential on the magnetic field (c). Fig. 9(a) shows an apparent correlation between NH_4^+ count sum and magnetic field magnitude, with a correlation coefficient of 0.55, confirming the apparent trend in Fig. 7. In particular, within the diamagnetic cavity ($B \approx 0$ nT), the count sum is very high (>200), while it is low (<100) for very high B magnitude ($B > 60$ nT). We also see that while Q was an important factor over large time-scales, over this small range, no dependence is observed. The dependence of NH_4^+ count sum with magnetic field is also not biased by the cometocentric distance over this period, as illustrated in Fig. 9(b), even when local outgassing derived from ROSINA/COPS is taken into account.

Due to lower electron temperature in the diamagnetic cavity (Odelstad et al. 2018), the spacecraft potential is typically around −10 V in this region (see Fig. 9c). More negative values of the spacecraft potential observed outside the diamagnetic cavity may accelerate ions out of the energy acceptance range of DFMS, meaning the detectability of positive ions decreases. This could generate a bias leading to stronger NH_4^+ detection inside the diamagnetic cavity. However, Fig. 9(d) shows that the NH_4^+ count sum is not correlated with the spacecraft potential. Hence, the correlation in Fig. 9(a) does not appear to be due to variation in the spacecraft potential.

Another possible reason for the trend of NH_4^+ with the magnetic field could be the deflection of ions out of the field of view of DFMS due to the presence of a magnetic field outside the diamagnetic cavity. To rule this out, we examine the count sums for two other ion species, for which the number density should not be governed by the likelihood of ion-neutral collisions. H_2O^+ should generally be at photochemical equilibrium at low enough cometocentric distances (Galand et al. 2016; Heritier et al. 2017). CH_3^+ does not undergo any significant ion-neutral chemical loss processes, and therefore its density should not vary systematically across the cavity boundary if the ion composition difference is due only to ion-neutral chemistry. Fig. 10 shows the count sums against magnetic field magnitude for these two species, where the colour scale shows the local outgassing. Fig. 10(a) shows that H_2O^+ has stronger than average counts inside the diamagnetic cavity, but there is no discernible trend with magnetic field strength as there is for NH_4^+. The correlation coefficient associated with H_2O^+ count sum for detected peaks versus the magnetic field strength is 0.17, compared to 0.55 for NH_4^+ in Fig. 9(a). This suggests that the trend in Fig. 9(a) is not driven purely by deflection out of the instrument field of view, as H_2O^+ and NH_4^+ have very similar masses, and we would therefore expect them to be affected similarly. This conclusion is confirmed by the absence of correlation between CH_3^+ counts and magnetic field strength (see Fig. 10b). Note that since 15 *m*/*z* is scanned three times less frequently than 18 *m*/*z*, statistics are low and there is only one scan of 15 *m*/*z* inside the cavity (see Table 2).

4.2 Overall trends in NH_4^+ with diamagnetic cavity crossings

Fig. 11 expands the previous analysis to all the days in which HR ion mode is active during a diamagnetic cavity crossing (see Table 2).

Fig. 11(a) shows the count sums of NH_4^+ as a function of the magnetic field magnitude, colour-coded by the local outgassing. This confirms the earlier findings from Section 4.1 (see Fig. 9): the highest count sums of NH_4^+ are associated with lower magnetic field magnitude, for a given range of local outgassing (high outgassing with $Q > 2 \times 10^{28}$ s^{-1} and moderate outgassing with $Q < 2 \times 10^{28}$ s^{-1}). As seen in Fig. 9(b), the count sum does not follow any trend in terms of cometocentric distance, even when the outgassing rate is taken into account.

4.3 Two key periods

With the link between NH_4^+ production and magnetic field established, we now focus on two periods in which the diamagnetic cavity was observed, and compare the observed NH_4^+ count sum to modelled ion density from the ionospheric model. The modelled outputs are calculated from the mean neutral composition and density averaged over the rotation period of the comet (see Section 2.3).

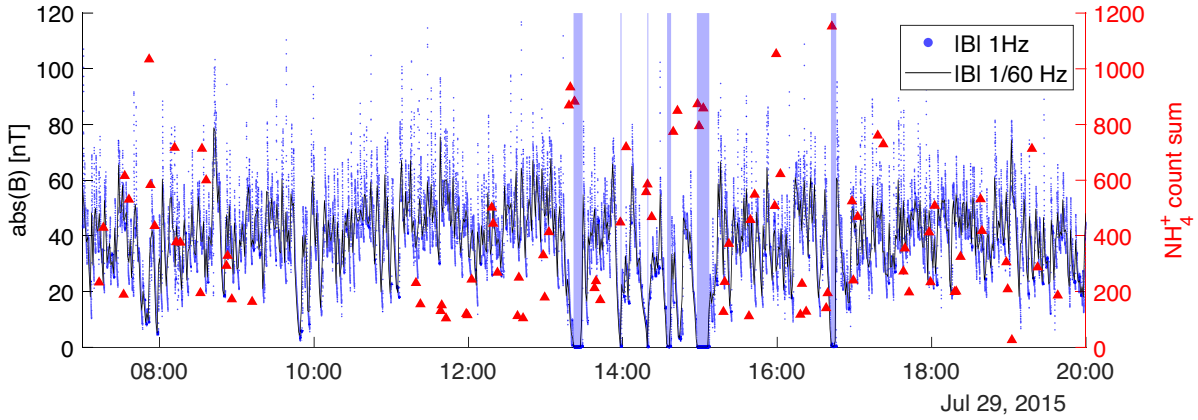

Figure 8. Time series (in UT) of the RPC/MAG magnetic field magnitude (blue dots 1 Hz, resampled to black line 1/60 Hz) and ROSINA/DFMS NH_4^+ detections (red triangles) on 2015 July 29. Diamagnetic cavity crossings are highlighted with violet vertical bars.

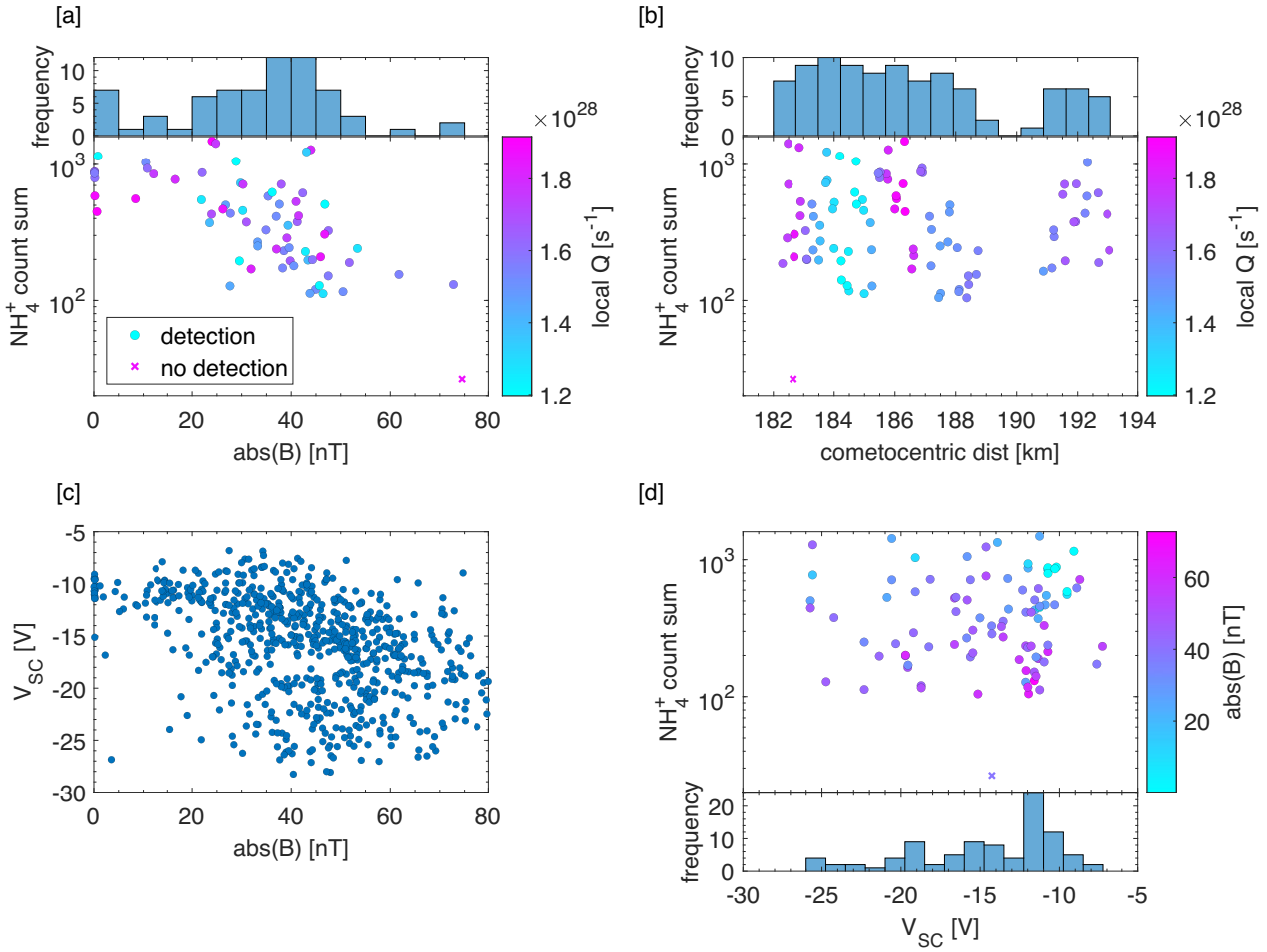

Figure 9. (a) ROSINA/DFMS NH_4^+ counts as a function of the magnetic field magnitude (RPC/MAG), and the colour scale shows the local outgassing Q. (b) NH_4^+ counts as a function of cometocentric distance. (c) Spacecraft potential as a function of magnetic field. All data are from 2015 July 29. (d) Counts as a function of spacecraft potential from RPC/LAP. Histograms for (a), (b), and (d) show the distribution of values for magnetic field, cometocentric distance, and spacecraft potential, respectively.

4.3.1 2015 July–August

First, we focus on 2015 July–August, which includes perihelion on 2015 August 13, and the most frequent scans of 18 *m/z* in HR ion mode. Fig. 12 shows how NH_3 and NH_4^+ detection varied over this period. The Northern hemisphere was in autumn (see Table 1). The local outgassing estimate is higher over the Southern hemisphere, as is the NH_3 number density.

Diamagnetic cavity crossings are shown by the vertical red dashed lines in Fig. 12(c), with the only scans of 18 *m/z* in HR ion mode inside

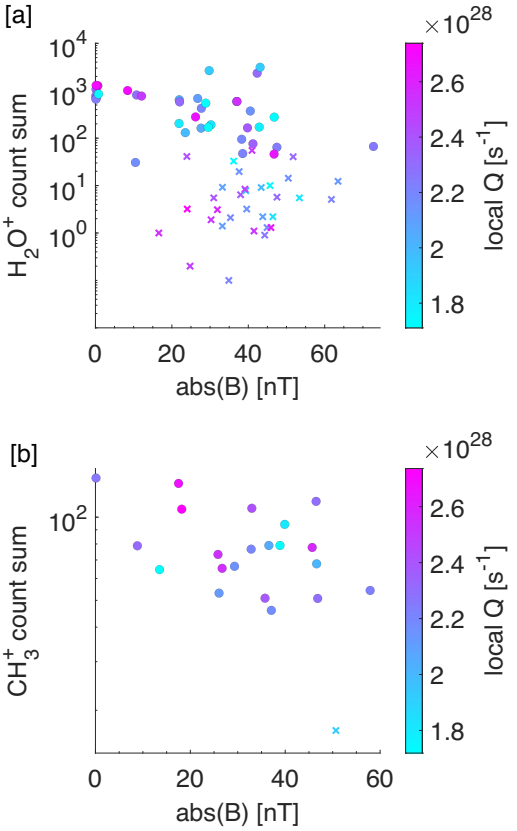

Figure 10. (a) Count sum against magnetic field magnitude with local outgassing colour scale for H_2O^+ and (b) CH_3^+ in HR ion mode. All data are from 2015 July 29.

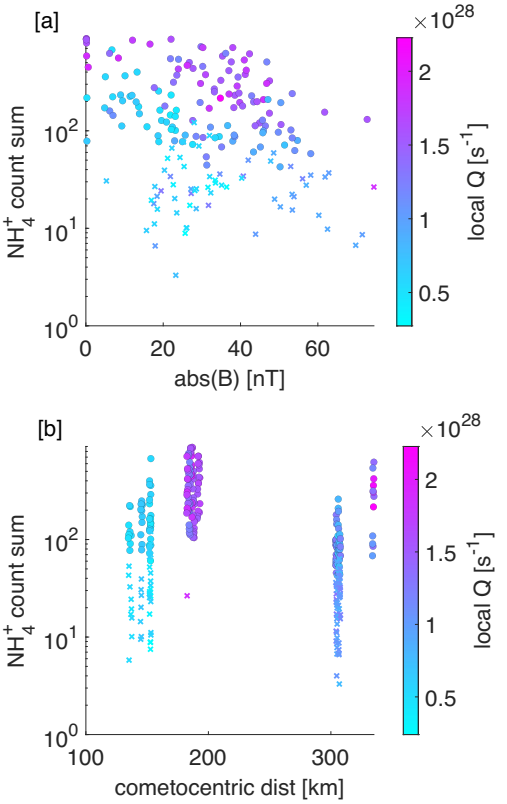

Figure 11. NH_4^+ count sum as a function of magnetic field (a) and cometocentric distance (b), with the colour scale showing the local outgassing. The data set is for the 6 d during which both DFMS was in HR ion data mode and a diamagnetic cavity was observed (see Table 2).

the cavity on 2015 July 29. It is clear that the NH_4^+ is particularly enhanced on this day, and that the local outgassing is not the main driver. For example, when comparing July 29 with August 1, the local outgassing and NH_3 density are similar but the NH_4^+ signal is much stronger when the diamagnetic cavity is present. In addition, in late August the NH_4^+ counts are very low, despite similar local outgassing to late July when we observe the enhanced counts. The counts peak again on August 22, when the diamagnetic cavity is again present and coinciding with HR ion mode (though no scans of 18 *m*/*z* take place inside the cavity on this day, see Table 2). Again, it seems that the presence of this ion species at perihelion is driven by the location of Rosetta relative to the diamagnetic cavity boundary. Note, however, that due to the unstable nature of the boundary, we cannot know the actual distance of Rosetta from the boundary at a given time (Goetz et al. 2016b).

The enhancement in the NH_4^+ density on July 29 is also predicted by ionospheric modelling (Fig. 12d) based on the ROSINA neutral density and composition at the Rosetta location (averaged over the 12.4-h rotation period of the comet) showing approximately a factor 1.5 increase between July 28 and July 29. The NH_4^+ is predicted to remain high until August 3. We also see that the proportion of NH_4^+ produced by NH_3 reacting with water group ions decreases during the enhancement. This suggests that NH_4^+ is being produced more readily through increased protonation of other HPA neutrals (e.g. H_2COH^+, $CH_3OH_2^+$, and H_3S^+), which is made possible by the higher local outgassing. More reactions can occur before the ion is lost through transport, so more chemical pathways are contributing to the production of NH_4^+. It is important to note that to apply the model, we assume that Rosetta is constantly within the diamagnetic cavity, and as such the model only captures ion composition driven by changes in local outgassing and neutral composition. It is therefore not sensitive to changing dynamics in different plasma interaction regions.

4.3.2 2015 November

Fig. 13 shows the same information as Fig. 12 but for 2015 November, when the largest number of ammonium salt dust grain impacts were observed (Altwegg et al. 2022). The signatures of NH_4^+ are generally weak or not present during this period but increase significantly on November 21 and remain high on November 25 and 28, despite no particular increase in NH_3 number density or mixing ratio. On November 21 and 25, NH_4^+ measurements coincide with times when Rosetta was within the diamagnetic cavity, and on November 28, Rosetta was sporadically within the cavity, hence likely close to the boundary when in HR ion mode. The enhanced NH_4^+ seems to be more driven by the presence of the diamagnetic cavity than the outgassing or NH_3 prevalence.

Fig. 13(d) shows the modelled NH_4^+ density for this period. The shaded region shows where the neutral density has been interpolated to fill the gap in the COPS coverage from November 18 to 21, assuming that the local outgassing is constant in this period. The NH_4^+ density then peaks on 2015 November 19, and begins to decrease on November 20. The modelled density then remains low, but detected counts are still high on November 25 and 28 when the diamagnetic cavity is present again. The relative contribution of reactions with

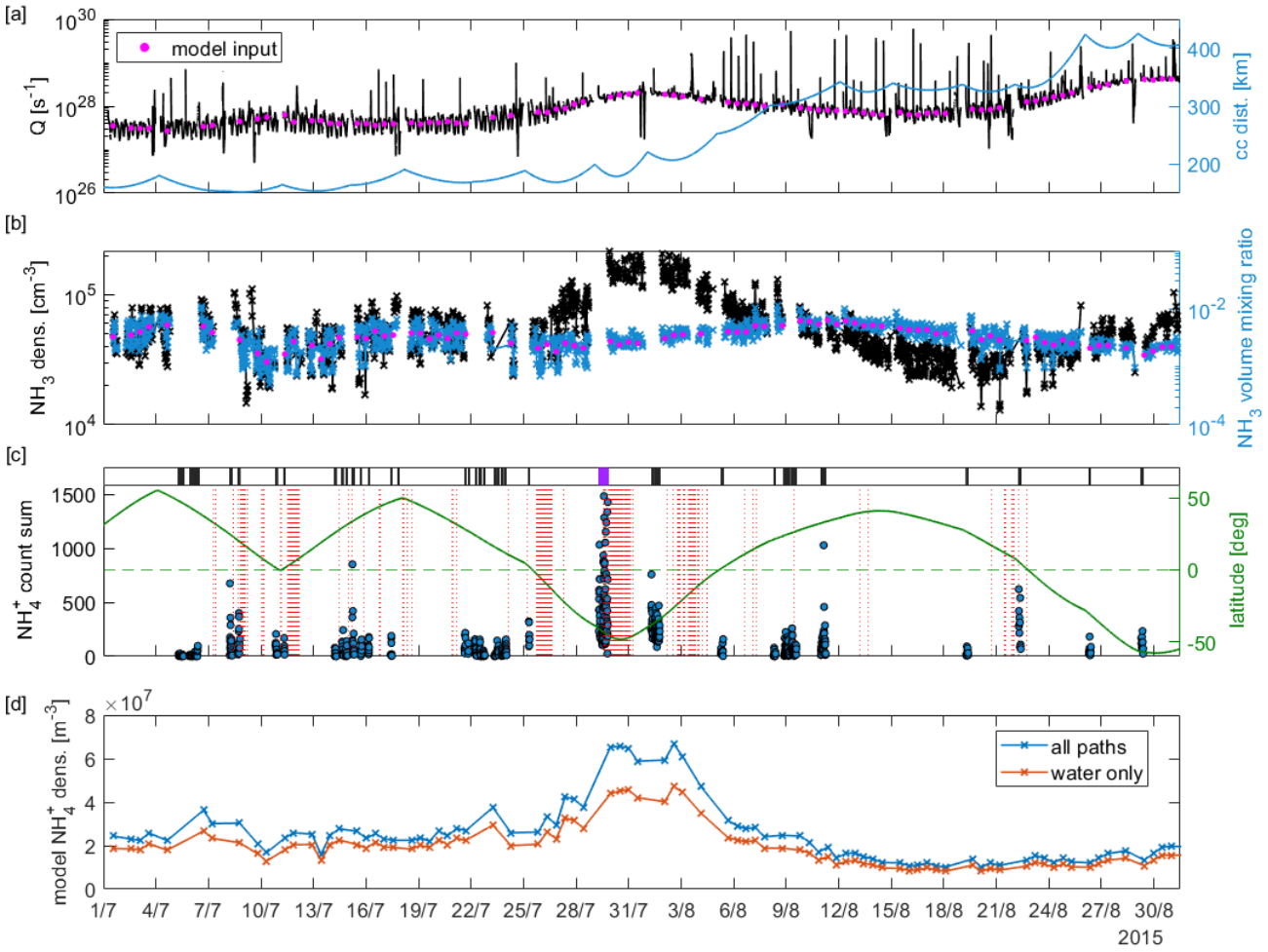

Figure 12. (a) Local outgassing from ROSINA/COPS (black), input outgassing used to generate model (pink), and cometocentric distance (blue). (b) NH_3 number density (black) and volume mixing ratio (blue, relative to total). Volume mixing ratio used as input to the model is shown in pink. (c) NH_4^+ count sum (blue), latitude (green), and diamagnetic cavity crossings (from RPC/MAG, vertical red lines). Black lines along the top show when DFMS HR ion mode is active, with purple highlighting 2015 July 29, on which the case study in Section 4.1 is based. (d) Modelled NH_4^+ ion density when all pathways to NH_4^+ (blue) and only water pathways (red) are 'switched on'.

water family ions decreases during the peak modelled ion density, and the peak corresponds to an increase in both the local outgassing and the NH_3 number density (but not the NH_3 mixing ratio).

Detection of NH_4^+ appears to be more strongly driven by the diamagnetic cavity than high outgassing over the full period analysed. Since the ionospheric model is only valid within the diamagnetic cavity with a radial flow of cometary ions, it is possible that the NH_4^+ count sum observed outside the cavity is reduced compared with the modelled density by increased acceleration and non-radial ion motion.

5 DISCUSSIONS AND CONCLUSIONS

First, we show that over the full course of ion mode observations (1.25–3.6 au), NH_4^+ detection frequency and count sums increase with local outgassing, and are most prevalent near perihelion, as are other HPA ions. Around perihelion in 2015 July and August, the detection is stronger over the Southern hemisphere, which is in spring during this period, and therefore has higher outgassing and a greater density of NH_3, due to greater insolation. NH_4^+ therefore has a source within the coma, and its presence is not reduced to spacecraft manoeuvres only. There are two candidates for the NH_4^+ source in the coma: ion-neutral chemistry (through protonation) and ammonium salt dust grain impacts.

While ammonium salts detected from dust grains (sublimating after impact inside the DFMS ion source) are mostly observed during post-perihelion over the Southern hemisphere, the majority of NH_4^+ detections happen around perihelion. The correlation between higher outgassing and NH_4^+ at perihelion is what we would expect from an ion-neutral chemistry source in the coma, and it remains the strongest candidate for the majority of detections observed. However, due to observational bias when looking for ammonium salts as a signal over background noise, it is likely that dust impacts are also more prevalent at perihelion when outgassing is higher (Altwegg et al. 2022). It is hence not possible to rule out that ammonium salt embedded in dust grains contributes as a source of NH_4^+ based on the analysis between its detection, local outgassing, and NH_3 (see Section 3).

Secondly, we find that for similar outgassing and cometocentric distances, the NH_4^+ signal is stronger inside the diamagnetic cavity than outside and appears to increase in prevalence with proximity to the diamagnetic cavity. More generally, the NH_4^+ count sum is found to increase with decreasing magnetic field strength (see Section 4.1).

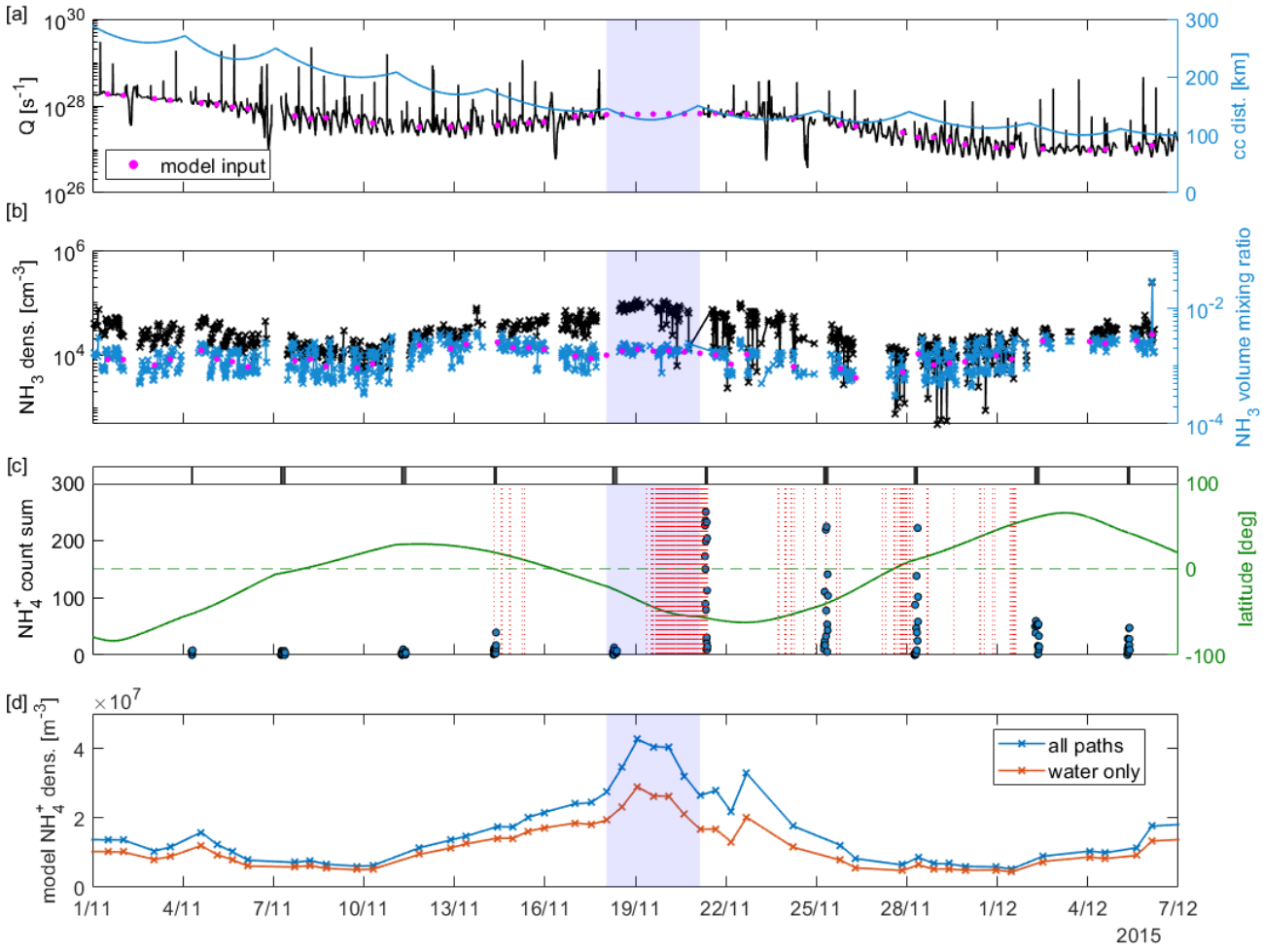

Figure 13. Same as Fig. 12, but for November 2015. The shaded region indicates where the neutral density has been interpolated to generate the ionospheric model inputs.

This trend is shown not to be driven by the less negative spacecraft potential inside the cavity. It is also not found for other ions of similar mass/charge, which do not undergo ion-neutral chemistry (i.e. CH_3^+), or even for H_2O^+ (which is at photochemical equilibrium), suggesting that the effect is not due to ion deflection out of the field of view by a stronger magnetic field.

We find by comparison with the ionospheric model that high NH_4^+ count sums appear more driven by the presence of the diamagnetic cavity than by favourable neutral conditions that increase the modelled NH_4^+ density (see Section 4.3). The model also predicts ion densities well above the estimated minimum detectable threshold of 5×10^4 m^{-3} (see Appendix A for derivation) for 2015 July, August, and November. This suggests that, since the model assumes to always be inside the diamagnetic cavity with a radial outflow of cometary ions, it overestimates the NH_4^+ prevalence outside the cavity. There, the flow is more dynamic and less radial, allowing less time for ion-neutral chemistry to take place. This is consistent with 3D hybrid simulations of the coma (e.g. Koenders et al. 2015), which show that the radial velocity dominates the flow inside the cavity, while there are more dynamics outside with a strong antisunward component.

We find a strong presence of NH_4^+ in early 2015 March (Section 3.1), following an increase in outgassing of around an order of magnitude during February (see Fig. 3a). The occurrence frequency and count sums are much higher in March than they are in 2015 May and June, when the local outgassing is similar, with lower neutral density measured by COPS in May due to higher cometocentric distance. Running the ionospheric model for the mean conditions on 2015 March 3 and 2015 May 13 predicts NH_4^+ ion densities of 1.40×10^7 and 1.54×10^7 m^{-3}, respectively. These are similar in magnitude to the modelled densities predicted for July, August, and November in Section 4.3, and suggest that detection is suppressed in May and June, rather than enhanced in March. It is possible that this is related to the presence or absence of a diamagnetic cavity around the comet. The cavity was detected throughout 2015 May and June, though all mass 18 observations by DFMS were made outside the cavity in this period. Based on our findings, the presence of a diamagnetic cavity would reduce the NH_4^+ density outside of it. If the cavity was not formed yet in 2015 March (which we speculate, but is consistent with its non-detection despite lower cometocentric distance in March than in 2015 May), the cometary ion flow would be expected to be more uniformly radial, as derived from multi-instrument analyses at lower activity (e.g. Galand et al. 2016, Heritier et al. 2018). In that case, we would expect higher NH_4^+ density in March than in May/June. This does not explain why a similar effect in terms of NH_4^+ was not observed in early 2016, when the comet moved away from perihelion again. There are, however, several detections of other HPA ions (H_2COH^+ and H_3S^+) in 2016 January–February, which may suggest some equivalence

to 2015 March, and at a similar heliocentric distance. There could potentially also be additional loss processes for NH_4^+ that are more efficient post-perihelion and in 2015 May/June than at other times, such as charge exchange with neutral metals (Aikin 1974) such as sodium (Beth et al. 2020). These topics all require further study.

In conclusion, the link between the detection of NH_4^+ and the local outgassing rate confirms that there is a source in the coma. While the protonation of NH_3 is a clear pathway, it is not possible to rule out a contribution from the dissociation of ammonium salts embedded in cometary dust grains sublimating near DFMS. The trend between the NH_4^+ count sum and the magnetic field strength suggests, however, that ion-neutral chemistry is the strongest driver at perihelion, and that the presence of NH_4^+ is influenced by ion dynamics outside the diamagnetic cavity. Improving our understanding of how the diamagnetic cavity behaves and how this impacts the *in situ* plasma data will be a crucial element of the upcoming Comet Interceptor mission (Snodgrass & Jones 2019).

ACKNOWLEDGEMENTS

We would like to acknowledge the invaluable work of the Rosetta Orbiter for Ion and Neutral Analysis (ROSINA) team, the Rosetta Plasma Consortium (including the Principle Investigator of RPC/MAG, K.-H. Glassmeier, and Principle Investigator of RPC/LAP, A. Eriksson), the whole ESA Rosetta team, and the ESA Planetary Science Archive team. Rosetta is an ESA mission with contributions from its member states and NASA. Work at Imperial College London was supported by the Science and Technology Facilities Council (STFC) of the UK under studentship ST/W507519/1 and grants ST/S000364/1 and ST/W001071/1, and by the UK Space Agency (UKSA) under grants ST/W002604/1 and ST/X002349/1. Work at the University of Bern was funded by the Canton of Bern and the Swiss National Science Foundation (200020_207312).

DATA AVAILABILITY

The data used in this article are available on the Planetary Science Archive (PSA) at https://psa.esa.int.

REFERENCES

Aikin A. C., 1974, ApJ, 193, 263
Altwegg K. et al., 1993, A&A, 279, 260
Altwegg K. et al., 2020, Nat. Astron., 4, 533
Altwegg K. et al., 2022, MNRAS, 516, 3900
Balsiger H. et al., 1986, Nature, 321, 330
Balsiger H. et al., 2007, Space Sci. Rev., 128, 745
Beth A. et al., 2016, MNRAS, 462, S562
Beth A. et al., 2020, A&A, 642, A27
Burch J. L., Goldstein R., Cravens T. E., Gibson W. C., Lundin R. N., Pollock C. J., Winningham J. D., Young D. T., 2007, Space Sci. Rev., 128, 697
Carr C. et al., 2007, Space Sci. Rev., 128, 629
Eriksson A. I. et al., 2007, Space Sci. Rev., 128, 729
Fougere N. et al., 2016, MNRAS, 462, S156
Galand M. et al., 2016, MNRAS, 462, S331
Gasc S. et al., 2017, MNRAS, 469, S108
Glassmeier K.-H. et al., 2007, Space Sci. Rev., 128, 649
Goetz C. et al., 2016a, MNRAS, 462, S459
Goetz C. et al., 2016b, A&A, 588, A24
Häberli R. M., Altwegg K., Balsiger H., Geiss J., 1995, A&A, 297, 881
Hänni N. et al., 2019, J. Phys. Chem. A, 123, 5805
Hässig M. et al., 2015, Science, 347, aaa0276
Henri P. et al., 2017, MNRAS, 469, S372
Heritier K. L. et al., 2017, MNRAS, 469, S427
Heritier K. L. et al., 2018, A&A, 618, A77
Koenders C., Glassmeier K. H., Richter I., Ranocha H., Motschmann U., 2015, Planet. Space Sci., 105, 101
Le Roy L. et al., 2015, A&A, 583, A1
Odelstad E., Stenberg-Wieser G., Wieser M., Eriksson A. I., Nilsson H., Johansson F. L., 2017, MNRAS, 469, S568
Odelstad E. et al., 2018, J. Geophys. Res. (Space Phys.), 123, 5870
Ostaszewski K. et al., 2021, Ann. Geophys., 39, 721
Rubin M., Hansen K. C., Gombosi T. I., Combi M. R., Altwegg K., Balsiger H., 2009, Icarus, 199, 505
Rubin M., Hansen K. C., Combi M. R., Daldorff L. K. S., Gombosi T. I., Tenishev V. M., 2012, J. Geophys. Res. (Space Phys.), 117, A06227
Schläppi B., 2011, PhD thesis. Physikalisches Institut der Universität Bern
Schläppi B. et al., 2010, J. Geophys. Res. (Space Phys.), 115, A12313
Snodgrass C., Jones G. H., 2019, Nat. Commun., 10, 5418
Stephenson P. et al., 2023, MNRAS , (submitted)
Vigren E., Galand M., 2013, ApJ, 772, 33

APPENDIX A: ESTIMATING A THRESHOLD FOR DETECTION OF AN ION SPECIES BY DFMS

The estimated ion density required for detection by DFMS used in Section 5 is calculated based on Schläppi (2011):

$$I_{\rm coma} = \frac{I_{\rm det}}{S_{\rm i}}, \tag{A1}$$

where $I_{\rm coma}$ is the current of ions of a given mass from the coma on to DFMS, $I_{\rm det}$ is the current reaching the detector, and $S_{\rm i}$ is the sensitivity of DFMS to the ion species, i. The current generated by one ion impacting at the detector during the integration dt is given by

$$I_{\rm det} = \frac{q}{{\rm d}t} = \frac{1.6 \times 10^{-19}\,{\rm C}}{20\,{\rm s}} \approx 1 \times 10^{-20}\,{\rm A}. \tag{A2}$$

Combining it with a typical sensitivity, of 5-eV ions of $^{20}Ne^+$ (of mass close to that of NH_4^+; Schläppi 2011), $S_{\rm i} \approx 5 \times 10^{-4}$, gives the current from the coma: $I_{\rm coma} = nvqA \approx 2 \times 10^{-17}$ A, where n is the ion number density of the species of interest (here, NH_4^+), v is its bulk velocity, and A is the collecting cross-section of DFMS (25.8 mm^2). As the bulk velocity of ions at 5 eV is

$$v = \sqrt{\frac{2E}{m}} \approx \sqrt{\frac{2 \times 5\,{\rm eV}}{20\,u}} \approx 7\,{\rm km\,s^{-1}}, \tag{A3}$$

the ion density is given by

$$n = \frac{I_{\rm coma}}{vqA} \approx \frac{2 \times 10^{-17}\,{\rm A}}{7\,{\rm km\,s^{-1}} \times 1.6 \times 10^{-19}\,{\rm C} \times 25.8\,{\rm mm^2}} \approx 0.001\,{\rm cm^{-3}}. \tag{A4}$$

As we require a count sum (counts summed ± 0.01 m/z on either side of the peak) of around 50 for a detection (see Fig. 2), this corresponds to a minimum density of 0.05 cm^{-3}.

This paper has been typeset from a TEX/LATEX file prepared by the author.